Ideal two-color field ratio for holographic angular streaking of electrons

D. Trabert,[1] A. Geyer,[1] N. Anders,[1] M. Hofmann,[1] M. S. Schöffler,[1] L. Ph. H. Schmidt,[1] T. Jahnke,[2] M. Kunitski,[1] R. Dörner,[1] and S. Eckart[1,*]

[1]*Institut für Kernphysik, Goethe-Universität, Max-von-Laue-Straße 1, 60438 Frankfurt am Main, Germany*

[2]*Max-Planck-Institut für Kernphysik, Saupfercheckweg 4, 69117 Heidelberg, Germany*

(Received 14 July 2023; accepted 14 November 2023; published 14 December 2023)

We study strong-field ionization of molecular hydrogen in highly intense corotating two-color laser fields. The measured electron momentum distributions show alternating half rings (AHRs) that are characteristic of subcycle interference. We report on the role of the two-color field ratio for the visibility of this subcycle interference. The ratio of the peak electric field at 780 nm compared to the peak electric field at 390 nm E_{780}/E_{390} is varied from 0.037 to 0.18. We find very good agreement with the results from our semiclassical simulation. We conclude that the AHR pattern is visible if two conditions are fulfilled. First, the amplitudes of the two pathways that lead to the subcycle interference have to be similar, which is the case for low two-color field ratios E_{780}/E_{390}. Second, the phase difference of the two pathways must be strong enough to allow for destructive interference, which is the case for high two-color field ratios E_{780}/E_{390}. For typical experimental conditions, we find that two-color field ratios E_{780}/E_{390} in the range from 0.037 to 0.12 lead to good visibility of the AHR pattern. This guides future experiments to measure the Wigner time delay using holographic angular streaking of electrons.

DOI: 10.1103/PhysRevResearch.5.043245

I. INTRODUCTION

When a highly intense laser pulse hits a single atom or molecule, an electron can be liberated by strong-field tunnel ionization [1]. The outgoing electronic wave packet can be described by a complex-valued wave function and carries information about the corresponding electronic bound state it emerged from [2–5] and the ionization dynamics [6–9]. The absolute square of the electronic wave function in momentum space is routinely measured [10]. In contrast, a full characterization of the electronic wave packet requires one to measure not only the electron wave packet's amplitude but also its phase. A very intriguing quantity that is closely related to the phase of the wave function is the Wigner time delay, which is defined as the derivative of the phase of the wave function with respect to the electron's energy [11,12]. In the single- and two-photon regimes, Wigner time delays were measured using reconstruction of attosecond beating by interference of two photon transitions (RABBITT) [13–16] and attosecond streaking [17,18] or from the interference pattern that is generated as the emitted photoelectron is diffracted by the parent ion's potential [12]. Recently, holographic angular streaking of electrons (HASE) has been introduced and it was demonstrated that it is the strong-field analog of RABBITT. Accordingly, HASE allows for the measurement of Wigner time delays in the strong-field regime [3,4,19]. This technique has been used previously to measure angle-resolved Wigner time delays in molecular photoionization processes [4,19]. HASE experiments are carried out using an ω-2ω bicircular corotating two-color (CoRTC) field that is composed of a strong 2ω component and a weak ω component. While RABBITT uses two-photon transitions and is modeled via a two-path interference in the energy domain, HASE is applied in the strong-field regime and is modeled via a two-path interference in the time domain. In previous works on HASE, the existence of the corresponding two-path subcycle interference in CoRTC fields has been demonstrated both theoretically and experimentally [3,20–22]. The characteristic interference pattern observed in the photoelectron momentum distribution is known as the alternating half ring (AHR) pattern and is a result of the interference between two electronic wave packets that are released within two half cycles of the ω component of the CoRTC field [22]. In the present work we show that two conditions are necessary to observe the AHR pattern. First, the two interfering wave packets must have similar amplitudes. Second, the phase difference for the subcycle interference must reach values up to π (otherwise destructive interference is not possible). The detailed mechanism leading to the AHR pattern in the electron momentum distribution has been already successfully described by HASE [3,22]. The key observable in HASE experiments is the rotation angle of the AHR pattern in the plane of polarization. Measuring this rotation angle allows for the retrieval of the electronic wave packet's phase gradient perpendicular to the tunnel exit in a momentum space representation. It should be noted that the AHR pattern is not sensitive to the ion dynamics that happens after ionization as HASE probes the properties of the electronic wave packet at the tunnel exit [4]. The ability

*eckart@atom.uni-frankfurt.de

to measure the electron's phase gradient is one of the key achievements of HASE and allows one to experimentally access Wigner time delays [3,4,19,23].

The aim of this joint experimental and theoretical work is to obtain a better and more detailed understanding of the underlying two-path interference leading to the emergence of the AHR pattern in the electron momentum distribution. To this end, we study the strong-field ionization of H_2 in CoRTC fields dominated by the 2ω component at a central wavelength of 390 nm and vary the intensity of the field at 780 nm. The basic principles that lead to the subcycle interference are discussed in Sec. II. In Sec. III the experimental techniques for light field synthesis and electron detection are described. We also describe how the intensity of the ω component at a central wavelength of 780 nm is varied (which modifies the two-color field ratio). The setup that is used to measure three-dimensional momentum distributions of all charged reaction fragments in coincidence is presented and the measured electron momentum distributions are discussed. The section is concluded by a detailed analysis of the AHR pattern's visibility as a function of the two-color field ratio. In Sec. IV we employ a trajectory-based semiclassical model to reproduce the experimentally obtained electron momentum distributions and to gain insight into the subcycle phase structure of the electronic wave function as well as the amplitude ratio of the two wave packets that contribute to the subcycle interference. In Sec. V the rotation angle of the AHR as a function of the electron emission direction relative to the internuclear axis of H_2 is investigated for different two-color field ratios. Atomic units (a.u.) are used throughout this work unless stated otherwise.

II. STRONG-FIELD IONIZATION IN COROTATING TWO-COLOR FIELDS

The shape of a two-path interference pattern depends on the amplitudes and the relative phases of the interfering wave packets. Subcycle interference patterns can be modeled [3,22,24,25] via two interfering wave packets using the following expression:

$$I(\Delta\Phi) = |A_1 e^{i\Phi_1} + A_2 e^{i(\Phi_1+\Delta\Phi)}|^2. \quad (1)$$

Here the intensity I depends on the relative phase $\Delta\Phi$ of the two waves and their amplitudes A_1 and A_2. The absolute phase Φ_1 does not affect the interference pattern. The modulation strength of the interference pattern is governed by the ratio of the amplitudes A_1 and A_2.

Figure 1 illustrates the temporal evolution of the electric field $\mathbf{E}(t)$ and the negative vector potential $-\mathbf{A}(t)$ in the plane of polarization (xy plane) for a single-color circularly polarized 2ω field [Fig. 1(a)] and a CoRTC field [Fig. 1(b)]. The green and the purple arrows in Fig. 1(b) visualize that each point in final momentum space can be reached by two combinations of negative vector potential and initial momentum at the tunnel exit. To understand why this is the case, one can describe the ionization as a two-step process. First, the electron tunnels through the classically forbidden region which results from the binding potential deformed by the instantaneous laser electric field. Second, the electron is subsequently accelerated in the combined electric field of the laser and the parent ion. Neglecting Coulomb interaction with the parent ion after tunneling, an electron which appears at the tunnel exit at a time t_0 reaches a final momentum $\mathbf{p}_{\text{elec}} = -\mathbf{A}(t_0) + \mathbf{p}_i$. Here $-\mathbf{A}(t_0)$ is the negative vector potential at the time t_0 and $\mathbf{p}_i$ is the initial momentum at the tunnel exit. For circularly polarized single-color fields it is often assumed that the component of $\mathbf{p}_i$ in the tunnel direction is negligible [26]. With this assumption, there remain only two possible combinations of $-\mathbf{A}(t_0)$ and $\mathbf{p}_i$ to reach a certain point in final momentum space [3].

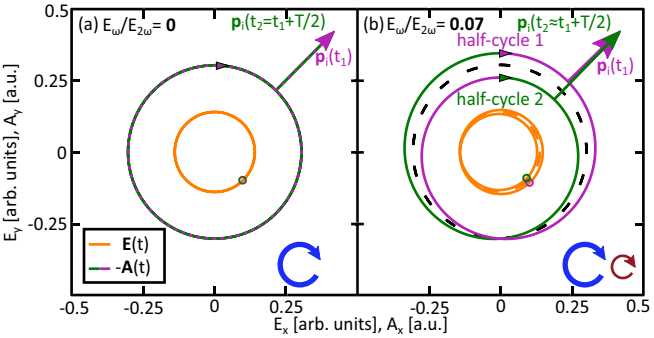

FIG. 1. Electric field and negative vector potential of a single color and a CoRTC field. (a) Lissajous curve for the electric field $\mathbf{E}(t)$ and the corresponding negative vector potential $-\mathbf{A}(t)$ for a circularly polarized 2ω light field with $E_{2\omega} = 0.035$ a.u. Each point in final momentum space can be reached by a well-defined initial momentum $\mathbf{p}_i$. The t_1 and t_2 fulfill the relation $t_2 = t_1 + T/2$. (b) Time-dependent electric field $\mathbf{E}(t)$ and negative vector potential $-\mathbf{A}(t)$ for a CoRTC field with a two-color field ratio $\frac{E_\omega}{E_{2\omega}} = 0.07$. Each point in final momentum space can be reached by two combinations of birth time $t_{1,2}$ and initial momentum $\mathbf{p}_i(t_{1,2})$. The t_1 and t_2 approximately fulfill the relation $t_2 \approx t_1 + T/2$. The negative vector potential that belongs to half cycle 1 (2) is represented by the purple (green) line. The electric field vectors that belong to the release times within the first (second) half cycle are indicated in purple (green).

Figure 1(a) shows the limiting case of a CoRTC field with a vanishing ω component (i.e., a single-color 2ω field). Within this limiting case, the two half cycles of the CoRTC field are exactly identical. Thus, there are two release times t_1 and $t_2 = t_1 + T/2$ per cycle T that lead to the same final electron momentum $\mathbf{p}_{\text{elec}}$. The initial momenta at the tunnel exit $\mathbf{p}_i(t_1) = \mathbf{p}_i(t_2)$ and the negative vector potentials $-\mathbf{A}(t_1) = -\mathbf{A}(t_2)$ are identical [illustrated by the green and purple arrows in Fig. 1(a)]. For this case, the phase difference between the two paths leading to $\mathbf{p}_{\text{elec}}$ is $\frac{1}{\hbar} I_p T/2$, where I_p denotes the ionization potential [27]. Further, the tunneling probability for any of the two half cycles is identical, corresponding to the special case $A_1 = A_2$ in Eq. (1) and thus allowing for perfect constructive and destructive interference in the final electron momentum distribution. In this case, the phase difference gives rise to interference maxima that are well known as above-threshold-ionization (ATI) peaks in the photoelectron energy distribution and do not produce any AHR pattern because the phase difference is independent of the electron release time and thus detection angle.

Figure 1(b) shows the combined electric field for a two-color field ratio $\frac{E_\omega}{E_{2\omega}}$ of 0.07, which is typical for previous experimental works [4,19,22]. For the two half cycles with

a duration of $T/2$, the electric field and the corresponding negative vector potential are not identical. In such a laser field, with a nonzero ω component, there are three major differences from the situation in a circularly polarized single-color 2ω field. First, the geometry is more complicated, since $-\mathbf{A}(t_0)$ is no longer perpendicular to $\mathbf{E}(t_0)$ for all release times t_0. The time between release time t_2 in the second half cycle and the release time t_1 in the first half cycle is now only approximately $t_1 + T/2$. The initial momentum which is needed to end up at a certain final electron momentum $\mathbf{p}_{\text{elec}}$ is different for the two half cycles (which is due to the differences of the negative vector potential). Second, the deviations in the relative release time from the exact $T/2$ periodicity and the difference in initial momentum lead to a more complicated evolution of the semiclassical phase. Thus, $\Delta\Phi$ can deviate from $\frac{I_p T}{2\hbar}$. Third, the ratio of amplitudes of the two interfering wave packets changes because $\mathbf{E}(t)$ varies on subcycle timescale and the tunneling probability depends on the magnitude of the laser electric field. This difference in amplitudes reduces the modulation strength of the interference pattern according to Eq. (1) and is illustrated by the different thicknesses of the green and purple arrows representing p_i in Fig. 1(b).

In order to unravel how the field ratio $\frac{E_\omega}{E_{2\omega}}$ effects the AHR pattern, different field ratios are compared. Figure 2(a) [Fig. 2(b)] shows the time-dependent electric field and negative vector potential of the smallest (largest) two-color field ratio of 0.037 (0.18) investigated in this work. While the splitting between the two half cycles is very small for the field depicted in Fig. 2(a), the field shown in Fig. 2(b) has a very large splitting and the ionization process can be expected to be dominated by the half cycle with the larger field amplitude. The measured electron momentum distributions in the plane of polarization (xy plane) are shown in Figs. 2(c) and 2(d) (see Sec. III for experimental details). In Fig. 2(c) the well-known AHR pattern can be clearly seen. In contrast, Fig. 2(d) shows that the AHR pattern can hardly been seen for the field ratio of $\frac{E_\omega}{E_{2\omega}} = 0.18$. In the remainder of this work, we will discuss why the AHR pattern is not seen for very low ratios $\frac{E_\omega}{E_{2\omega}}$, appears for ratios on the order of 0.037, and vanishes again for high field ratios.

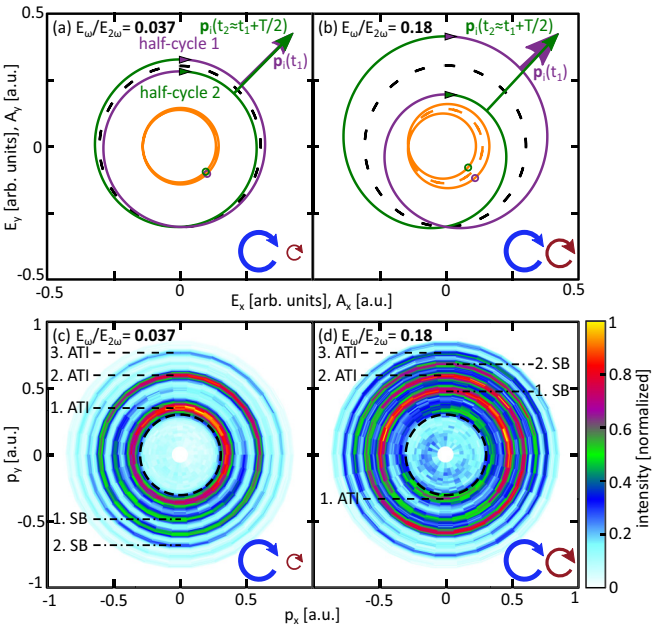

FIG. 2. Electric field and negative vector potential of CoRTC fields with varying two-color field ratios and corresponding measured electron momentum distributions. (a) Time-dependent electric field $\mathbf{E}(t)$ and negative vector potential $-\mathbf{A}(t)$ of a CoRTC field with $E_{2\omega} = 0.035$ a.u. and a two-color field ratio of $\frac{E_\omega}{E_{2\omega}} = 0.037$. (b) Same as in (a) but for a two-color field ratio of $\frac{E_\omega}{E_{2\omega}} = 0.18$. The negative vector potential of half cycle 1 (2) is represented by the purple (green) line. The electric fields corresponding to the release times within the first (second) half cycle are indicated by purple (green) circles. (c) Measured electron momentum distribution in the plane of polarization (xy plane) for $\frac{E_\omega}{E_{2\omega}} = 0.037$. A weakly modulated AHR pattern is visible. The ATI and SB peaks are labeled. (d) Same as in (c) but for $\frac{E_\omega}{E_{2\omega}} = 0.18$. Here the AHR pattern is less pronounced. The dashed circles in all panels show the negative vector potential for the circularly polarized single-color field shown in Fig. 1(a).

III. EXPERIMENTAL DETAILS AND ANALYSIS OF MEASURED ELECTRON MOMENTUM DISTRIBUTIONS

To generate the CoRTC fields used in our experiment, laser pulses at a fundamental frequency ω (wavelength of 780 nm) are frequency doubled using a 200-μm β-barium-borate crystal, resulting in laser pulses at a frequency 2ω. The setup is the same as in [4,7,22,28]. A dichroic beam splitter separates the two frequency components such that the intensity and the polarization of the ω and the 2ω pulses can be set independently. A piezoelectric delay stage allows us to ensure temporal overlap and to control the relative phase of the two single-color laser pulses that form the CoRTC field. The resulting two-color laser pulses are focused by a spherical mirror (focal length $f = 75$ mm) onto a cold supersonic jet of hydrogen molecules resulting in an intensity (peak electric field) of 8.4×10^{13} W/cm^2 ($E_{2\omega} = 0.035$ a.u.) for the 2ω component of the CoRTC field. A gradient neutral density filter is used to set 12 different intensities (peak electric fields) for the ω component ranging from 1.4×10^{11} W/cm^2 ($E_\omega = 0.0014$ a.u.) to 2.8×10^{12} W/cm^2 ($E_\omega = 0.0064$ a.u.). This leads to two-color field ratios between $\frac{E_\omega}{E_{2\omega}} = 0.037$ and 0.18. The intensity calibration is done by comparing the envelopes from Figs. 3(f)–3(j) with our semiclassical simulation that uses initial conditions at the tunnel exit from strong-field approximation (SFA) as in Refs. [4,7]. After ionization, electrons and ionic fragments are guided by static electric and static magnetic fields towards the position- and time-sensitive detectors of a cold target recoil ion spectroscopy reaction microscope [29]. Each detector is comprised of a double stack of microchannel plates and hexagonal delay-line anodes [30]. The ion (electron) arm of the spectrometer has a length of 66 mm (390 mm), an electric field of 10.9 V/cm, and a magnetic field of 8.1 G. The time-of-flight direction of the spectrometer is perpendicular to the jet direction and both directions lie in the polarization plane (xy plane). The z direction is the light propagation direction. The three-dimensional momentum vectors of all charged particles are measured in coincidence. The relative phase between the two single-color laser pulses is

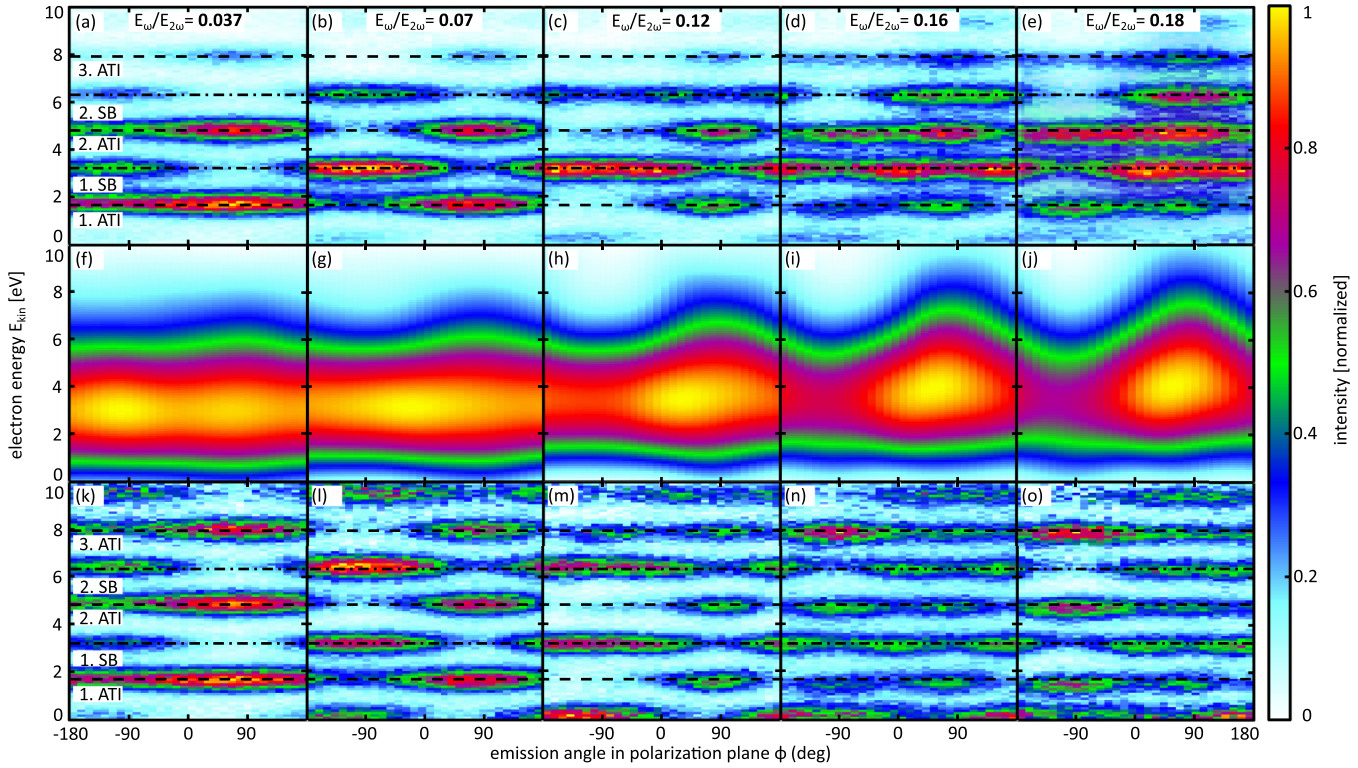

FIG. 3. Measured electron energy distributions for varying CoRTC field ratios $\frac{E_\omega}{E_{2\omega}}$. (a)–(e) Measured electron momentum distributions as a function of the angle $\phi = \arctan2(p_y, p_x)$ and the energy $E_{\text{kin}} = \frac{p_x^2+p_y^2+p_z^2}{2}$ for two-color field ratios $\frac{E_\omega}{E_{2\omega}}$ from 0.037 to 0.18. The three ATI (two SB) peaks visible are indicated by dashed (dash-dotted) lines. (f)–(j) Envelopes (low-pass-filtered distribution to remove the modulation due to the photon energy; see the text) extracted from the measured distributions shown in (a)–(e). For larger field ratios, a stronger modulation of the angular distribution is observed. (k)–(o) Interference patterns obtained by dividing the measured distributions shown in (a)–(e) by the corresponding envelopes shown in (f)–(j) for each bin separately. The emergence and the breakdown of the AHR pattern can be observed. (l) Most symmetric AHR pattern.

continuously scanned during the experiment. This allows us to compensate for slow drifts in the offline analysis by a rotation of the momentum distribution in the polarization plane. For the present work, single ionization followed by dissociation of the hydrogen molecule is studied. Each event in the electron momentum distributions is measured in coincidence with a single H^+ ion released via the reaction $H_2 \rightarrow H + H^+ + e^-$.

To further analyze electron momentum distributions as in Figs. 2(c) and 2(d), we calculate the electron's kinetic energy $E_{\text{kin}} = \frac{p_x^2+p_y^2+p_z^2}{2}$ and its emission angle in the plane of polarization $\phi = \arctan2(p_y, p_x)$. Figures 3(a)–3(e) show the measured electron energy distributions as a function of these two quantities for some of the measured two-color field ratios $\frac{E_\omega}{E_{2\omega}}$. The three ATI peaks and the two sideband (SB) peaks that are relevant in the further discussion are indicated by the dashed and dash-dotted lines. In analogy to Ref. [4], we disentangle the observed pattern into a product of an envelope function [Figs. 3(f)–3(j)] and the underlying AHR pattern [Figs. 3(k)–3(o)]. The envelope function is obtained by suppressing Fourier components in the energy distribution corresponding to the modulation that is due to the photon energy and higher frequencies while ensuring that the integral for each bin along ϕ does not change. This produces the experimentally obtained envelopes that are depicted in Figs. 3(f)–3(j). The modulation strength of the angular distribution increases for higher intensities of the ω component as expected due to the nonlinearity of the tunneling probability as a function of the magnitude of the laser's electric field. For the field ratios 0.12, 0.16, and 0.18 [Figs. 3(h)–3(j)], the most probable kinetic energy increases due to the increasing magnitude of the negative vector potential of the dominant half cycle. The experimental data have been rotated in the plane of polarization such that the most probable electron emission angle (integrated over the electron's energy) qualitatively agrees with the one obtained from the semiclassical simulation (see Sec. IV). For the simulation, the maximum splitting in the negative vector potential is at $\phi = 90°$, as illustrated in Figs. 1(b), 2(a), and 2(b).

For a two-color field ratio of 0.037 [Fig. 3(k)], the SB peaks are only weakly populated but show a strong angular modulation. For a two-color field ratio of 0.07 [Fig. 3(l)], the ATI and SB peaks are equally populated and show a similar angular modulation strength. This is the two-color field ratio used in previous works that applied the HASE technique to experimentally investigate the Wigner time delay [4,19]. Higher field ratios as in Figs. 3(l)–3(o) increase the population of the SB peaks compared to the ATI peaks.

In order to conduct a more quantitative discussion, we calculate the discrete Fourier transform of the angular distributions as in Figs. 3(k)–3(o) for each energy peak. Figure 4(a) shows the ratio of the onefold symmetric component F_1 and the integral dc component F_0. For a circularly polarized

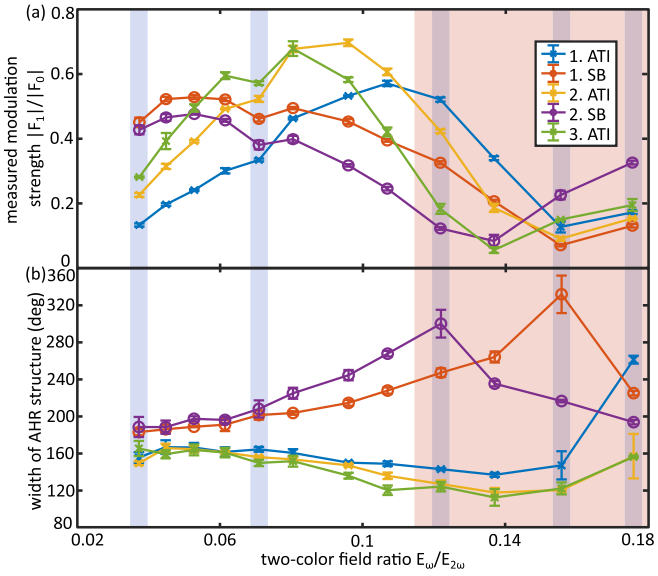

FIG. 4. Measured modulation strength (AHR visibility) and width of the AHR pattern. (a) Visibility of the AHR pattern as a function of the two-color field ratio $\frac{E_\omega}{E_{2\omega}}$. Here the visibility is expressed as the modulation strength, which in turn is given by the ratio between the onefold symmetric component F_1 and the dc component F_0 of the discrete Fourier transform of the angular distribution for each energy peak. (b) Width (FWHM; see the text) of the AHR pattern for each energy peak as a function of the two-color field ratio $\frac{E_\omega}{E_{2\omega}}$. Data points corresponding to ATI (SB) peaks are indicated by crosses (circles). The data points within the blue shaded areas indicate the field ratios shown in more detail in Fig. 3. The red area highlights field ratios for which the AHR pattern shows more than a single peak [but also double peaks, e.g., for the first SB of Fig. 3(n)]. Error bars show the statistical error only.

single-color pulse, as illustrated in Fig. 1(a), this quantity would be zero. Figure 4(a) shows that for the smallest two-color field ratio of 0.037, the onefold symmetric modulation is much stronger for the SB than for the ATI peaks. The reason for this is obvious when looking at Fig. 3(k). While the modulation of the SB peaks is ideal for small two-color field ratios, the angular distributions corresponding to the ATI peaks remain rather isotropic. For increasing two-color field ratios, the Fourier component F_1 increases for the ATI peaks and eventually reaches its maximum at slightly different field ratios for the individual energy peaks. For the two SB peaks, F_1/F_0 remains rather constant up to a two-color field ratio of around 0.1 and then decreases rapidly. The red area in Fig. 4 highlights two-color field ratios for which the angular distributions for the energy peaks are not dominated by single peaks [as, e.g., for the first SB of Fig. 3(n)].

The difference in the intensity comparing the ATI versus the SB peaks in Fig. 4(a) is in qualitative agreement with the expectation from the photon picture. In the photon picture (i.e., in the energy domain that is used to interpret RABBITT experiments), the AHR pattern on the SB is caused by an interference between two channels: one channel for which N photons at 2ω are absorbed and one photon at ω is absorbed and the other channel for which $N+1$ photons at 2ω are absorbed and one photon at ω is emitted (stimulated emission). As soon as the transition amplitude for absorption and emission of one ω photon becomes appreciable, the sidebands arise in an energy region that was empty before. The increased intensity on the sideband manifests as a depletion for the main energy peak that belongs to a certain ATI peak. For these main energy peaks the modulation is often small compared to the signal of the entire peak (which also exists without the ω field). Although the photon picture can be used to qualitatively understand certain features of the AHR pattern, it is complicated to model all phase shifts in the energy domain and relies on the assumption that the ω field can be treated perturbatively [31]. For our scenario this is not the case because the ω field modulates the birth times of the electrons significantly [3]. The semiclassical approach, which is used for the remainder of this paper, does not rely on this assumption and reproduces the AHR pattern as a two-path interference in the time domain [3,22]. Thus, we will use this semiclassical time-domain modeling (Sec. IV), which fully consistently models our findings without the need to invoke the photon picture (energy domain perspective) as done in RABBITT.

Figure 4(b) shows the angular width of the AHR pattern as a function of the two-color field ratio for each energy peak. To obtain this quantity, the one-dimensional angular distributions were low-pass filtered for each energy peak. There are usually two angles for which these smoothed curves yield half of the maximum modulation strength as a function of the emission angle. The distance between those angles is shown in the figure as the width of the AHR pattern and corresponds to the full width at half maximum (FWHM). For low two-color field ratios, it is close to 180°. For the SB peaks, the width increases with the field ratio, while for the ATI peaks, the width decreases. This effect can be clearly seen by comparing Figs. 3(k) and 3(m). Our results are in line with previous theoretical works investigating linearly polarized two-color fields [25]. Note that for field ratios that are within the red area in Fig. 4, the peak width cannot be unambiguously determined.

IV. INVESTIGATION OF TWO-PATH INTERFERENCE USING OUR SEMICLASSICAL MODEL

To better understand the origin of the two-path interference that gives rise to the AHR pattern for CoRTC fields, we use a semiclassical trajectory-based model [32]. It is similar to the semiclassical two-step model [27] but uses initial conditions at the tunnel exit from strong-field approximation [33] as in [8,34] and also includes the semiclassical phase associated with each classical trajectory which enables the modeling of interference in final momentum space.

For our semiclassical simulations, we include Coulomb interaction after tunneling between the electron and the parent ion. It is important to note that SFA predicts a nonzero initial momentum component parallel to the tunnel exit direction, when the magnitude of the laser's electric field changes as a function of time (as is the case for CoRTC fields with a nonvanishing ω component). For our simulations, we use a two-cycle flat-top CoRTC pulse with a peak electric field of 0.037 a.u. for the 2ω component and field ratios of 0, 0.037, 0.07, 0.12, and 0.18. The peak electric field of the 2ω component is chosen such that the envelope in Fig. 5(g) has the same most probable energy as in Fig. 3(f). The

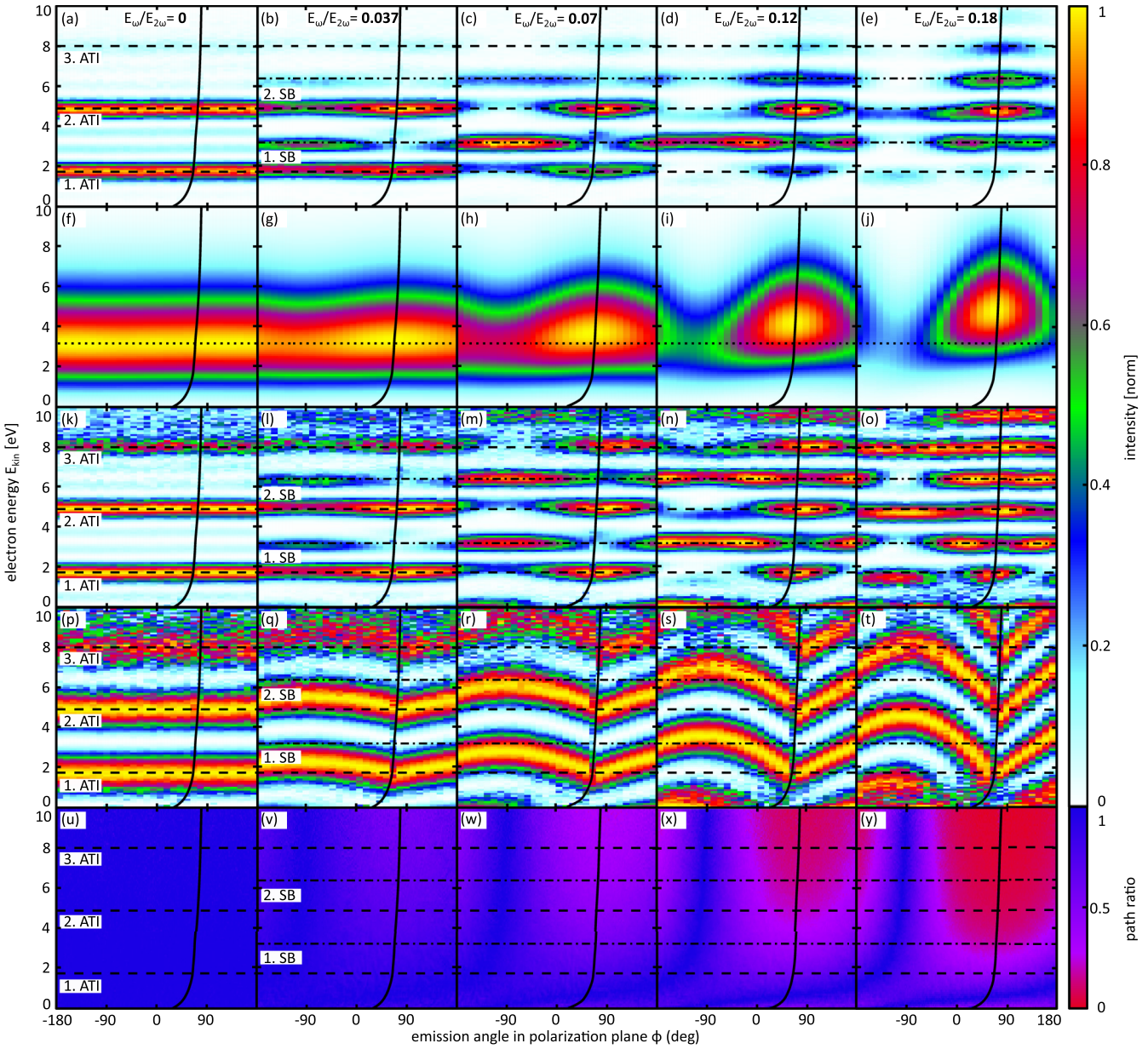

FIG. 5. Analysis of the two-path subcycle interference using the semiclassical model. (a)–(e) Results from the full semiclassical simulations as a function of $E_{\rm kin}$ and ϕ for two-color field ratios from 0 to 0.18 as indicated in the panels. In analogy to Eq. (1), this can be expressed via $|\sum_{n=1}^{4} A_n \exp(i\Phi_n)|^2$. (f)–(j) Same as in (a)–(e), but here the four simulated electron trajectories, which are launched during all four half cycles, are added up incoherently to suppress interference, which can be written as $\sum_{n=1}^{4} |A_n|^2$. The dotted horizontal line indicates the most probable energy for the single-color 2ω field with an peak electric field of 0.035 a.u. (k)–(o) Normalized coherent sum which can be expressed as $\frac{|\sum_{n=1}^{4} A_n \exp(i\Phi_n)|^2}{\sum_{n=1}^{4} |A_n|^2}$ in full analogy to the row above. The ATI (SB) peaks are indicated by the dashed (dash-dotted) lines. (p)–(t) Subcycle interference pattern $|\exp(\Phi_1) + \exp(\Phi_2)|^2$ between the first two half cycles. (u)–(y) Path ratio $1 - |\frac{A_1 - A_2}{A_1 + A_2}|$ for the subcycle two-path interference. The curved black lines indicate the transition between half cycles 1 (3) and 2 (4).

ionization potential $I_{\rm p}$ of 16.17 eV is used, which leads to good agreement of the energy peaks in Fig. 5(l) with the peaks in Fig. 3(k) and is consistent with the expectation for the non-Franck-Condon transition in strong-laser fields [35,36].

For the further analysis, the amplitudes $A_{1,2,3,4}$ and the phases $\Phi_{1,2,3,4}$ of the semiclassical electronic wave function in final momentum space are discussed for values $t_{1,2,3,4}$ of t_0 in the four half cycles of the flat-top part of the pulse that is used for the simulation. This allows for the calculation of incoherent intensity distributions as well as for the modeling of subcycle and intercycle interference patterns in full analogy to the discussion in Ref. [3].

Figures 5(a)–5(e) show the results of our semiclassical simulations for several field ratios in full analogy to the experimental results [see Figs. 3(a)–3(e)]. Based on Eq. (1), this can be expressed via $|\sum_{n=1}^{4} A_n \exp(i\Phi_n)|^2$. We find

good agreement of the semiclassical simulations with the experimental results.

Figures 5(f)–5(j) show the incoherent sum $\sum_{n=1}^{4}|A_n|^2$ of electron trajectories launched during all four half cycles. The result can be compared with the envelopes extracted from the experimental data shown in Figs. 3(f)–3(j). The angle-dependent energy distributions are in very good agreement with the experimental observations. The simulated modulation strength of the angular distribution is slightly more pronounced in our simulation compared to the experiment. The narrower energy distribution for a given value of ϕ can be explained by the focal averaging which is inherently present in the experiment but is not included in our simulation. The curved black line is the same in all panels of Fig. 5 and guides the eye, indicating the transition from the first (third) to the second (fourth) half cycle. The line's curvature is a result of an energy-dependent attoclock offset angle which is due to Coulomb interaction between the electron and the parent ion after tunneling [8,37,38].

Figures 5(k)–5(o) show the normalized coherent sum $\frac{|\sum_{n=1}^{4}A_n\exp(i\Phi_n)|^2}{\sum_{n=1}^{4}|A_n|^2}$ over all four half cycles in the flat-top part of the pulse. This is equivalent to the normalized measured interference patterns shown in Figs. 3(k)–3(o). As before, the ATI (SB) peaks are indicated by dashed (dash-dotted) lines. The simulated interference patterns are in very good qualitative agreement with their measured counterparts.

In the next and final step of this section, the amplitudes and the phase structure of the subcycle wave packets are discussed. To this end, we consider one full cycle of the CoRTC comprised of the first half cycle and the second half cycle only. Figures 5(p)–5(t) show the subcycle interference $|\exp(\Phi_1)+\exp(\Phi_2)|^2$ considering only the phase difference and neglecting amplitudes. For the case of a circularly polarized single-color laser field, the CoRTC subcycle interference is just identical to the 2ω intercycle interference, exhibiting ATI peaks spaced by the energy $2\hbar\omega$ independent of the angle ϕ [see Fig. 5(p)]. For a nonzero ω component [see Figs. 5(q)–5(t)], the interference pattern has the shape of arcs that extend farther in the energy direction for increasing two-color field ratios. These arcs are the underlying reason for the observation of the AHR pattern [3,22]. Additionally, intercycle interference leads to discrete final electron energies [indicated by the dashed and dash-dotted horizontal lines in Figs. 5(q)–5(t)] and thus cuts out arc segments leading to the AHR pattern. For the smallest nonzero two-color field ratio of 0.037, the arcs are only weakly bent [see Fig. 5(l)] and hence lead to intense ATI peaks compared to relatively weak SB peaks.

For larger two-color field ratios, the arcs are so strongly bend that a twofold symmetric angular distribution can emerge for certain energy peaks (see, e.g., the last column of Fig. 5). Although the subcycle interference for a two-color field ratio of 0.18 predicts destructive interference for the SB peaks around $\phi = 90^\circ$ [see Fig. 5(t)], the full interference pattern shown in Fig. 5(e) has no clear minimum because the envelope dominates [see Fig. 5(j)]. This hints at the second important aspect in the formation of the AHR pattern: Unequal amplitudes A_1 and A_2 limit the achievable modulation strength of the subcycle interference.

In order to quantify the ratio of the amplitudes of the two wave packets that lead to the subcycle interference, we define the path ratio as $1-|\frac{A_1-A_2}{A_1+A_2}|$. Accordingly, the path ratio has the value of 1 if $A_1 = A_2$ and the value of 0 if either $\frac{A_1}{A_2}$ or $\frac{A_2}{A_1}$ goes to zero. This quantity is shown in Figs. 5(u)–5(y). For the single-color 2ω field, A_1 and A_2 are independent of $E_{\rm kin}$ and ϕ [see Fig. 5(u)]. For all other cases around $\phi = 90^\circ$, where the splitting in the negative vector potential and the corresponding electric field between the two half cycles is at its maximum, the path ratio reaches its minimum. For a two-color field ratio of 0.18, the path ratio is close to zero for a wide range of combinations of $E_{\rm kin}$ and ϕ [see Fig. 5(y)]. The only exception is the region around $\phi = -90^\circ$, where the shape of the negative vector potential and the corresponding electric field is almost independent of the two-color field ratio and is similar to a single-color 2ω field. This is supported by the energy spacing of $2\hbar\omega$ that can be observed around $\phi = -90^\circ$ in Fig. 5(o). At the same time, the electric field leading to a relevant ionization probability has an effective periodicity which is ω, leading to an energy spacing of only $\hbar\omega$ [see $\phi = 90^\circ$ in Fig. 5(e)]. Thus, our semiclassical simulation provides a clear and quantitative understanding why the AHR pattern vanishes for low and high two-color field ratios.

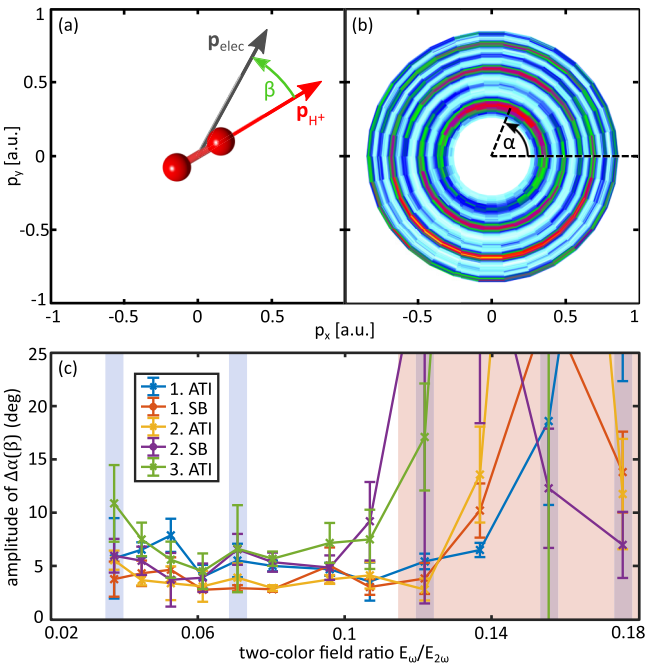

FIG. 6. Rotation of the AHR pattern as a function of the two-color field ratio for the reaction $H_2 \rightarrow H + H^+ + e^-$. (a) Definition of β as the angle between the final electron momentum $\mathbf{p}_{\rm elec}$ and the momentum vector $\mathbf{p}_{H^+}$ of the proton in the light's plane of polarization. (b) Definition of the angle α indicating the most probable electron emission direction for each ATI (SB) peak in the plane of polarization. (c) Amplitude of the sinusoidal dependence of $\Delta\alpha$ on β as a function of the two-color field ratio. The blue areas indicate the field ratios shown in more detail in Fig. 3 and are the same as in Fig. 4. The red area is the same as in Fig. 4. Error bars in (b) show the statistical error only.

V. ROTATION OF THE AHR PATTERN AS A FUNCTION OF THE ELECTRON EMISSION DIRECTION RELATIVE TO THE INTERNUCLEAR AXIS OF H_2

In this section we analyze how a central observable in HASE experiments, namely, the rotation angle α [see Fig. 6(a)], depends on the two-color field ratio. This rotation angle α allows one to measure the energy- and angle-resolved Wigner time delays upon the strong-field ionization of molecules [4]. Using the same approach and data analysis technique as in Ref. [4], we divide the full data set into subsets for different relative angles β. Here β is the angle between the electron's momentum vector $\mathbf{p}_{\text{elec}}$ and the proton's momentum vector $\mathbf{p}_{\text{H}^+}$ for the reaction $\text{H}_2 \rightarrow \text{H} + \text{H}^+ + e^-$ [see Fig. 6(a)].

For a given value of β, the electron momentum distribution in the plane of polarization is obtained. After demerging the envelope and the interference pattern as for the third row of Fig. 3, the rotation angle α for each ATI and SB peak can be determined [see Fig. 6(b)]. This is done for all values of β to obtain $\alpha(\beta)$. Subtracting the mean value α_{mean} from $\alpha(\beta)$ for each ATI and SB peak, one obtains the quantity $\Delta\alpha(\beta)$, which can be directly associated with phase gradients in momentum space perpendicular to the tunnel exit [3,4]. An approximately sinusoidal curve shape of $\Delta\alpha(\beta)$ is typically observed [4]. In the final step of this work, we quantify the influence of the two-color field ratio on the observable $\Delta\alpha(\beta)$. To this end, we determine the amplitude of the sinusoidal dependence as a function of the two-color field ratio. The result is shown in Fig. 6(c). Within the statistical uncertainty, the value remains constant for all field ratios outside the red area (i.e., two-color field ratios at which the AHR is clearly visible). This leads to the conclusion that the HASE technique works even if the field ratio is varied by a factor of 3 with respect to the two-color field ratio at which the AHR is most pronounced (corresponds to a change in intensity of the ω component by an order of magnitude).

VI. CONCLUSION

In this joint experimental and theoretic study we have investigated the alternating half ring pattern observed for CoRTC fields dominated by the 2ω component. We found that the AHR pattern is visible for two-color field ratios E_{780}/E_{390} in the range from 0.037 to 0.12 for typical experimental conditions (ionization of molecular hydrogen and an intensity on the order of 10^{14} W/cm^2). For higher field ratios the AHR pattern, which is a subcycle interference pattern, cannot be observed because only one of the two wave packets, which contributes to the subcycle interference, has a relevant amplitude. For very low field ratios, the phase differences for the two path interference is independent of the electron's release time and reproduces the well-known ATI peaks for a single-color field at 2ω. Our findings show why a field ratio E_{780}/E_{390} of 0.06–0.07 was chosen in previous experiments [4]. Finally, our results should lead to a comprehensive and quantitative understanding of the AHR pattern and are of practical significance for HASE experiments, as they identify a region of two-color field ratios that allow for the application of the HASE technique and the retrieval of Wigner time delays.

ACKNOWLEDGMENTS

This work was supported by the DFG (German Research Foundation) through Priority Programme SPP 1840 QUTIF. M.H. acknowledges funding from the DFG (Project No. 328961117) SFB 1319 ELCH (Extreme light for sensing and driving molecular chirality). We acknowledge fruitful discussions with Simon Brennecke and Manfred Lein.

[1] M. V. Ammosov, N. B. Delone, and V. P. Krainov, Tunnel ionization of complex atoms and of atomic ions in an alternating electromagnetic field, Sov. Phys. JETP **0664**, 1191 (1986).

[2] A. Staudte, S. Patchkovskii, D. Pavičić, H. Akagi, O. Smirnova, D. Zeidler, M. Meckel, D. M. Villeneuve, R. Dörner, M. Y. Ivanov, and P. B. Corkum, Angular tunneling ionization probability of fixed-in-space H_2 molecules in intense laser pulses, Phys. Rev. Lett. **102**, 033004 (2009).

[3] S. Eckart, Holographic angular streaking of electrons and the Wigner time delay, Phys. Rev. Res. **2**, 033248 (2020).

[4] D. Trabert, S. Brennecke, K. Fehre, N. Anders, A. Geyer, S. Grundmann, M. S. Schöffler, L. P. H. Schmidt, T. Jahnke, R. Dörner, M. Kunitski, and S. Eckart, Angular dependence of the Wigner time delay upon tunnel ionization of H_2, Nat. Commun. **12**, 1697 (2021).

[5] M. Meckel, D. Comtois, D. Zeidler, A. Staudte, D. Pavičić, H. C. Bandulet, H. Pépin, J. C. Kieffer, R. Dörner, D. M. Villeneuve, and P. B. Corkum, Laser-induced electron tunneling and diffraction, Science **320**, 1478 (2008).

[6] L. Arissian, C. Smeenk, F. Turner, C. Trallero, A. V. Sokolov, D. M. Villeneuve, A. Staudte, and P. B. Corkum, Direct test of laser tunneling with electron momentum imaging, Phys. Rev. Lett. **105**, 133002 (2010).

[7] S. Eckart, K. Fehre, N. Eicke, A. Hartung, J. Rist, D. Trabert, N. Strenger, A. Pier, L. P. H. Schmidt, T. Jahnke, M. S. Schöffler, M. Lein, M. Kunitski, and R. Dörner, Direct experimental access to the nonadiabatic initial momentum offset upon tunnel ionization, Phys. Rev. Lett. **121**, 163202 (2018).

[8] D. Trabert, N. Anders, S. Brennecke, M. S. Schöffler, T. Jahnke, L. P. H. Schmidt, M. Kunitski, M. Lein, R. Dörner, and S. Eckart, Nonadiabatic strong field ionization of atomic hydrogen, Phys. Rev. Lett. **127**, 273201 (2021).

[9] O. Kneller, D. Azoury, Y. Federman, M. Krueger, A. J. Uzan, G. Orenstein, B. D. Bruner, O. Smirnova, S. Patchkovskii, M. Ivanov, and N. Dudovich, A look under the tunnelling barrier via attosecond-gated interferometry, Nat. Photon. **16**, 304 (2022).

[10] J. Ullrich, R. Moshammer, A. Dorn, R. Dörner, L. P. H. Schmidt, and H. Schmidt-Böcking, Recoil-ion and electron momentum spectroscopy: Reaction-microscopes, Rep. Prog. Phys. **66**, 1463 (2003).

[11] E. P. Wigner, Lower limit for the energy derivative of the scattering phase shift, Phys. Rev. **98**, 145 (1955).

[12] J. Rist, K. Klyssek, N. M. Novikovskiy, M. Kircher, I. Vela-Pérez, D. Trabert, S. Grundmann, D. Tsitsonis, J. Siebert, A. Geyer *et al.*, Measuring the photoelectron emission delay in the molecular frame, Nat. Commun. **12**, 6657 (2021).

[13] P. M. Paul, E. S. Toma, P. Breger, G. Mullot, F. Augé, P. Balcou, H. G. Muller, and P. Agostini, Observation of a train of attosecond pulses from high harmonic generation, Science **292**, 1689 (2001).

[14] H. G. Muller, Reconstruction of attosecond harmonic beating by interference of two-photon transitions, Appl. Phys. B **74**, s17 (2002).

[15] J. Vos, L. Cattaneo, S. Patchkovskii, T. Zimmermann, C. Cirelli, M. Lucchini, A. Kheifets, A. S. Landsman, and U. Keller, Orientation-dependent stereo Wigner time delay and electron localization in a small molecule, Science **360**, 1326 (2018).

[16] M. Swoboda, T. Fordell, K. Klünder, J. M. Dahlström, M. Miranda, C. Buth, K. J. Schafer, J. Mauritsson, A. L'Huillier, and M. Gisselbrecht, Phase measurement of resonant two-photon ionization in helium, Phys. Rev. Lett. **104**, 103003 (2010).

[17] E. Constant, V. D. Taranukhin, A. Stolow, and P. B. Corkum, Methods for the measurement of the duration of high-harmonic pulses, Phys. Rev. A **56**, 3870 (1997).

[18] M. Schultze, M. Fieß, N. Karpowicz, J. Gagnon, M. Korbman, M. Hofstetter, S. Neppl, A. L. Cavalieri, Y. Komninos, T. Mercouris, C. A. Nicolaides, R. Pazourek, S. Nagele, J. Feist, J. Burgdörfer, A. M. Azzeer, R. Ernstorfer, R. Kienberger, U. Kleineberg, E. Goulielmakis *et al.*, Delay in photoemission, Science **328**, 1658 (2010).

[19] D. Trabert, N. Anders, A. Geyer, M. Hofmann, M. S. Schöffler, L. P. H. Schmidt, T. Jahnke, M. Kunitski, R. Dörner, and S. Eckart, Angular dependence of the Wigner time delay upon strong-field ionization from an aligned *p* orbital, Phys. Rev. Res. **5**, 023118 (2023).

[20] M. Han, P. Ge, Y. Shao, Q. Gong, and Y. Liu, Attoclock photoelectron interferometry with two-color corotating circular fields to probe the phase and the amplitude of emitting wave packets, Phys. Rev. Lett. **120**, 073202 (2018).

[21] P. Ge, M. Han, Y. Deng, Q. Gong, and Y. Liu, Universal description of the attoclock with two-color corotating circular fields, Phys. Rev. Lett. **122**, 013201 (2019).

[22] S. Eckart, D. Trabert, K. Fehre, A. Geyer, J. Rist, K. Lin, F. Trinter, L. P. H. Schmidt, M. S. Schöffler, T. Jahnke, M. Kunitski, and R. Dörner, Sideband modulation by subcycle interference, Phys. Rev. A **102**, 043115 (2020).

[23] S. Brennecke, Electron momentum distributions from strong-field-induced ionization of atoms and molecules, Ph.D. thesis, Leibniz University Hannover, 2023.

[24] D. G. Arbó, K. L. Ishikawa, K. Schiessl, E. Persson, and J. Burgdörfer, Intracycle and intercycle interferences in above-threshold ionization: The time grating, Phys. Rev. A **81**, 021403(R) (2010).

[25] Y. Feng, M. Li, S. Luo, K. Liu, B. Du, Y. Zhou, and P. Lu, Semiclassical analysis of photoelectron interference in a synthesized two-color laser pulse, Phys. Rev. A **100**, 063411 (2019).

[26] H. Ni, U. Saalmann, and J.-M. Rost, Tunneling ionization time resolved by backpropagation, Phys. Rev. Lett. **117**, 023002 (2016).

[27] N. I. Shvetsov-Shilovski, M. Lein, L. B. Madsen, E. Räsänen, C. Lemell, J. Burgdörfer, D. G. Arbó, and K. Tőkési, Semiclassical two-step model for strong-field ionization, Phys. Rev. A **94**, 013415 (2016).

[28] S. Eckart, M. Richter, M. Kunitski, A. Hartung, J. Rist, K. Henrichs, N. Schlott, H. Kang, T. Bauer, H. Sann, L. P. H. Schmidt, M. Schöffler, T. Jahnke, and R. Dörner, Nonsequential double ionization by counterrotating circularly polarized two-color laser fields, Phys. Rev. Lett. **117**, 133202 (2016).

[29] R. Dörner, V. Mergel, O. Jagutzki, L. Spielberger, J. Ullrich, R. Moshammer, and H. Schmidt-Böcking, Cold target recoil ion momentum spectroscopy: A 'momentum microscope' to view atomic collision dynamics, Phys. Rep. **330**, 95 (2000).

[30] O. Jagutzki, A. Cerezo, A. Czasch, R. Dörner, M. Hattas, M. Huang, V. Mergel, U. Spillmann, K. Ullmann-Pfleger, T. Weber, H. Schmidt-Böcking, and G. D. W. Smith, Multiple hit readout of a microchannel plate detector with a three-layer delay-line anode, IEEE Trans. Nucl. Sci. **49**, 2477 (2002).

[31] L. J. Zipp, A. Natan, and P. H. Bucksbaum, Probing electron delays in above-threshold ionization, Optica **1**, 361 (2014).

[32] S. Brennecke, N. Eicke, and M. Lein, Gouy's phase anomaly in electron waves produced by strong-field ionization, Phys. Rev. Lett. **124**, 153202 (2020).

[33] S. V. Popruzhenko, G. G. Paulus, and D. Bauer, Coulomb-corrected quantum trajectories in strong-field ionization, Phys. Rev. A **77**, 053409 (2008).

[34] A. Geyer, D. Trabert, M. Hofmann, N. Anders, M. S. Schöffler, L. P. H. Schmidt, T. Jahnke, M. Kunitski, R. Dörner, and S. Eckart, Experimental fingerprint of the electron's longitudinal momentum at the tunnel exit in strong field ionization, Phys. Rev. Res. **5**, 033094 (2023).

[35] P. Dietrich, M. Y. Ivanov, F. A. Ilkov, and P. B. Corkum, Two-electron dissociative ionization of H_2 and D_2 in infrared laser fields, Phys. Rev. Lett. **77**, 4150 (1996).

[36] J. H. Posthumus, The dynamics of small molecules in intense laser fields, Rep. Prog. Phys. **67**, 623 (2004).

[37] P. Eckle, A. N. Pfeiffer, C. Cirelli, A. Staudte, R. Dörner, H. G. Muller, M. Büttiker, and U. Keller, Attosecond ionization and tunneling delay time measurements in helium, Science **322**, 1525 (2008).

[38] A. W. Bray, S. Eckart, and A. S. Kheifets, Keldysh-Rutherford model for the attoclock, Phys. Rev. Lett. **121**, 123201 (2018).